Chapter 5

Thin Wires

In this chapter we will use the Method of Moments to analyze the radiation and scattering by thin, conducting wires. This is an area of great practical interest, as many realistic antennas can be modeled by wires whose radius is much smaller than their length and the operating wavelength. We first develop the thin-wire approximation to the magnetic vector potential and introduce the Hallén and Pocklington integral equations for straight wires. We then discuss practical feed models, including the delta-gap and magnetic-frill models, and apply the electric field integral equation (EFIE) to wires of arbitrary shape. We will then present several examples with geometries having more general, realistic configurations.

5.1 Thin Wire Approximation

Consider a perfectly conducting long, $\hat{\mathbf{z}}$-oriented thin wire of length L whose radius a is much less than L and λ. An incident electric field $\mathbf{E}^i(\mathbf{r})$ excites a surface current $\mathbf{J}(\mathbf{r})$ on this wire. As the wire is very thin, we assume that $\mathbf{J}(\mathbf{r})$ is a filamentary electric current $I_z(\mathbf{r})$ which can be written as

$$\mathbf{J}(\mathbf{r}) = \frac{I_z(z)}{2\pi a}\hat{\mathbf{z}}\,, \tag{5.1}$$

where there is no dependence on the wire azimuthal angle ϕ. We also assume that the current goes to zero at the wire ends and that no current flows onto the end caps. In cylindrical coordinates, we can write the corresponding magnetic vector potential A_z as

$$A_z(\rho,\phi,z) = \mu\int_{-L/2}^{L/2}\int_0^{2\pi}\frac{I_z(z')}{2\pi}\frac{e^{-jkr}}{4\pi r}\,d\phi'\,dz'\,, \tag{5.2}$$

where

$$r = |\mathbf{r}-\mathbf{r}'| = \sqrt{(z-z')^2+|\boldsymbol{\rho}-\boldsymbol{\rho}'|^2}\,. \tag{5.3}$$

Using the fact that $\rho' = a$, using the law of cosines we then write

$$|\boldsymbol{\rho}-\boldsymbol{\rho}'|^2 = \rho^2+a^2-2\rho a\cos(\phi'-\phi)\,. \tag{5.4}$$

As the integrand is a function of $\phi' - \phi$, the result is cylindrically symmetric. As a result, we can replace $\phi' - \phi$ with ϕ' and write

$$A_z(\rho, z) = \mu \int_{-L/2}^{L/2} \frac{I_z(z')}{2\pi} \int_0^{2\pi} \frac{e^{-jkr}}{4\pi r}\, d\phi'\, dz' \,, \tag{5.5}$$

where

$$r = \sqrt{(z - z')^2 + \rho^2 + a^2 - 2\rho a \cos\phi'} \,, \tag{5.6}$$

and the integral

$$\int_0^{2\pi} \frac{e^{-jkr}}{4\pi r}\, d\phi' \tag{5.7}$$

is referred to as the cylindrical wire kernel in the literature [1, 2]. If we assume a to be very small, we can approximate r as

$$r = \sqrt{(z - z')^2 + \rho^2} \,, \tag{5.8}$$

and the innermost integral is no longer a function of ϕ', resulting in

$$A_z(\rho, z) = \mu \int_{-L/2}^{L/2} I_z(z') \frac{e^{-jkr}}{4\pi r}\, dz' \,. \tag{5.9}$$

The above is commonly referred to as the *thin wire approximation* with *reduced kernel*. The original surface integral has been replaced by a line integral along the axis of the wire. In cases where the dimensions of the problem invalidate the assumptions of the reduced kernel, the cylindrical wire kernel should be evaluated more accurately, for example using the methods in [3]. Using (3.73), the radiated electric field is then

$$-j\omega \Big[1 + \frac{1}{k^2} \frac{\partial^2}{\partial z^2}\Big] A_z = E_z^s \,. \tag{5.10}$$

For a perfectly conducting wire, the total tangential electric field on the wire surface is zero. Therefore, we can now write the above in terms of the incident field E_z^i

$$j\omega \Big[1 + \frac{1}{k^2} \frac{\partial^2}{\partial z^2}\Big] A_z = E_z^i \,. \tag{5.11}$$

When solving the thin wire problems in this chapter, we will assume the testing points are located on the axis of the wire and the source points to be on the surface. We also note that (5.11) comprises a simplified version of (3.181) where $\mathbf{M} = 0$.

There are two common ways to write (5.11). The first retains the differential operator outside the integral, and is

$$j\omega\mu \Big[1 + \frac{1}{k^2} \frac{\partial^2}{\partial z^2}\Big] \int_{-L/2}^{L/2} I_z(z') \frac{e^{-jkr}}{4\pi r}\, dz' = E_z^i(z) \,. \tag{5.12}$$

This is called *Hallén's integral equation* [4]. We can also move the differential operator under the integral sign, yielding

$$j\omega\mu \int_{-L/2}^{L/2} I_z(z') \Big[1 + \frac{1}{k^2} \frac{\partial^2}{\partial z^2}\Big] \frac{e^{-jkr}}{4\pi r}\, dz' = E_z^i(z) \,, \tag{5.13}$$

which is called *Pocklington's integral equation* [5]. Pocklington's equation is generally less convenient in a numerical sense, as the differential operator acts directly on the Green's function. As we will see, this formulation typically converges more slowly and can be less accurate than the corresponding Hallén formulation when simple pulse basis functions and point matching are used.

5.2 Thin Wire Excitations

In antenna problems, the unknowns of interest are usually the input impedance at the feedpoint and the resulting radiation pattern, directivity, and gain. The easiest way to compute these is to consider the antenna in its transmitting mode, which requires a reasonable model of the feed system at the input terminals. Practically, the antenna might be fed by an open-wire transmission line, or by a coaxial line through a ground plane. These various feed systems impact the antenna impedance characteristics in different ways. With this in mind, we need a way to model the field introduced by the feed system without having to model the system itself. In this section we consider two common feed methods used in thin wire problems, the delta-gap source and the magnetic frill. The delta-gap source assumes that the field due to the feedline exists only in the gap between the antenna terminals, with a value of zero outside (no fringing effects). This is a simple method that typically produces less accurate results for input impedance, but still performs well in computing radiation patterns. The magnetic frill models the feed as a coaxial line that terminates in a monopole over a ground plane. It generally yields a more realistic input impedance, at the cost of additional computation when assembling the right-hand-side vector.

5.2.1 Delta-Gap Source

The delta-gap source model assumes the impressed electric field in the thin gap between the antenna terminals can be expressed as

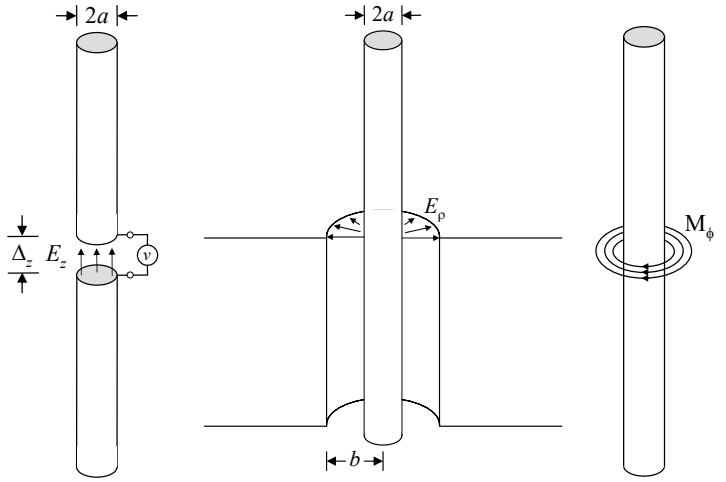
$$\mathbf{E}^i = \frac{V_0}{\Delta_z}\hat{\mathbf{z}}\,, \tag{5.14}$$

where Δ_z is the width of the gap, and V_0 is the voltage across the gap. This is illustrated in Figure 5.1a. In most practical implementations, the gap exists in only the feed segment and $\mathbf{E}^i$ is zero on all other segments. The excitation vector therefore has nonzero contributions from only those basis functions that overlap the feed segment.

5.2.2 Magnetic Frill

In Figure 5.1b, we depict a coaxial line feeding a monopole antenna over an infinite ground plane. If the aperture field is assumed to be purely TEM, the method of images allows the ground plane and aperture to be replaced by the equivalent magnetic frill shown in Figure 5.1c. With an aperture electric field given by

$$\mathbf{E}(\rho) = \frac{1}{2\rho\log(b/a)}\hat{\boldsymbol{\rho}}\,, \tag{5.15}$$



(a) Delta-Gap (b) Coaxial Line Feeding Monopole (c) Frill

Figure 5.1: Thin Wire Excitation Models

the equivalent magnetic current density is

$$\mathbf{M}(\rho) = -2\,\hat{\mathbf{n}} \times \mathbf{E}(\rho) = \frac{-1}{\rho \log(b/a)}\hat{\boldsymbol{\phi}} \qquad a \le \rho \le b\,. \tag{5.16}$$

This equivalent magnetic current produces an electric field along the wire. For a frill centered at the origin, the axial field on the wire axis ($\rho = 0$) is [6]

$$E_z^i(z) = \frac{1}{2\log(b/a)}\left(\frac{e^{-jkR_1}}{R_1} - \frac{e^{-jkR_2}}{R_2}\right), \tag{5.17}$$

where

$$R_1 = \sqrt{z^2 + a^2} \tag{5.18}$$

and

$$R_2 = \sqrt{z^2 + b^2}\,. \tag{5.19}$$

The $\hat{\mathbf{z}}$-directed field in (5.17) is the incident field used for the right-hand side vector. Note that in using this model, we are effectively modeling a dipole with the feed system of a monopole. A true monopole will have an input impedance only half that of the dipole as it only radiates into the half space above the ground.

The axial electric-field amplitude for a frill with $a = 1$ mm, $b = 5$ mm, and $\lambda = 1$ m is shown in Figure 5.2. Given the sharp drop-off of the field near $z = 0$, when computing the right-hand side vector elements special attention should be paid to the numerical integration so that maximum accuracy is obtained.

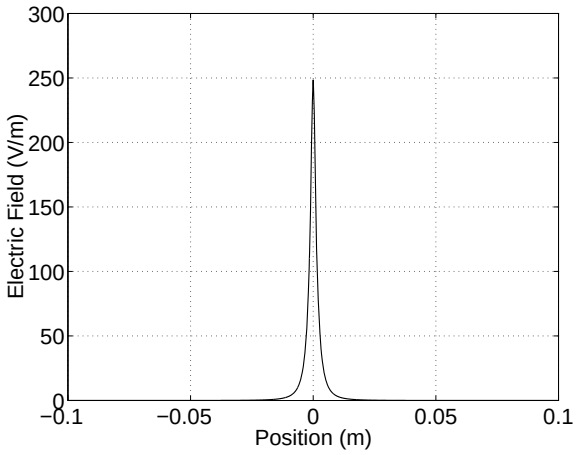


Figure 5.2: Field Intensity Due To Frill

5.2.3 Plane Wave

The tangential electric field on a filamentary wire can be written as

$$E_{tan}(\mathbf{r}) = \hat{\mathbf{t}}(\mathbf{r}) \cdot \mathbf{E}(\mathbf{r}) \,, \tag{5.20}$$

where $\hat{\mathbf{t}}(\mathbf{r})$ is the vector tangent to the wire at $\mathbf{r}$. For a $\hat{\mathbf{z}}$-oriented wire illuminated by a $\hat{\boldsymbol{\theta}}$-oriented plane wave of unit amplitude incident from direction $\hat{\mathbf{r}}^i$, (5.20) becomes

$$E_{tan}(\mathbf{r}) = \hat{\mathbf{z}} \cdot \hat{\boldsymbol{\theta}}\, e^{-jk\mathbf{r}\cdot\hat{\mathbf{r}}^i} = \sin\theta^i e^{jkz\cos\theta^i} \,. \tag{5.21}$$

Because the thin-wire approximation assumes no azimuthally excited currents, a $\hat{\phi}$-polarized incident wave will induce no current on the wire.

5.3 Hallén's Equation

We will now consider the solution to Hallén's equation (5.12). If we write it as

$$j\omega\Big[1 + \frac{1}{k^2}\frac{\partial^2}{\partial z^2}\Big] A_z(z) = E_z^i(z) \,, \tag{5.22}$$

we see that it is an inhomogeneous scalar Helmholtz equation for $A_z(z)$, which can be solved by the Green's function method. The general solution to the homogeneous equation

$$\Big[1 + \frac{1}{k^2}\frac{\partial^2}{\partial z^2}\Big] A_z(z) = 0 \tag{5.23}$$

is

$$A_z(z) = C_1 e^{jkz} + C_2 e^{-jkz} \,. \tag{5.24}$$

To obtain a particular solution we must obtain the Green's function $G(z)$ which satisfies the equation

$$j\omega\Big[1+\frac{1}{k^2}\frac{\partial^2}{\partial z^2}\Big]G(z)=\delta(z)\;. \tag{5.25}$$

Once $G(z)$ is known, the solution for $A_z(z)$ can be obtained by

$$A_z(z)=C_1e^{jkz}+C_2e^{-jkz}+\int_{-L/2}^{L/2}G(z,z')\;E_z^i(z')\;dz'\;. \tag{5.26}$$

To obtain the Green's function, let us use the trial function

$$G(z)=C\sin(k|z|)\;, \tag{5.27}$$

which is continuous at $z=0$ with discontinuous derivative at $z=0$ as is required for the Green's function [7]. To determine the constant C, we integrate (5.25) from $-\epsilon$ to ϵ, yielding

$$j\omega C\int_{-\epsilon}^{\epsilon}\sin(k|z|)\;dz-\frac{j\omega}{k}C[\cos(-kz)]\Big|_{-\epsilon}^{0}+\frac{j\omega}{k}C[\cos(kz)]\Big|_{0}^{\epsilon}=1\;. \tag{5.28}$$

If we allow ϵ to approach zero, the first term goes to zero and after evaluating the remaining terms we get

$$C=-\frac{jk}{2\omega}=-\frac{j\mu}{2\eta}\;. \tag{5.29}$$

Thus,

$$G(z)=-\frac{j\mu}{2\eta}\sin(k|z|)\;, \tag{5.30}$$

and the solution for $A_z(z)$ is

$$A_z(z)=C_1e^{jkz}+C_2e^{-jkz}-\frac{j\mu}{2\eta}\int_{-L/2}^{L/2}\sin(k|z-z'|)\;E_z^i(z')\;dz'\;. \tag{5.31}$$

Substituting the original expression for A_z on the left-hand side of the above yields

$$\begin{aligned}\int_{-L/2}^{L/2}I_z(z')\frac{e^{-jkr}}{4\pi r}\;dz'&=C_1e^{jkz}+C_2e^{-jkz}\\&\quad-\frac{j}{2\eta}\int_{-L/2}^{L/2}\sin(k|z-z'|)\;E_z^i(z')\;dz'\;.\end{aligned} \tag{5.32}$$

By similar reasoning, a second solution for the Green's function is

$$G_z(z)=\frac{\mu}{2\eta}e^{-jk|z|}\;, \tag{5.33}$$

leading to a second expression for A_z, which is

$$\int_{-L/2}^{L/2}I_z(z')\frac{e^{-jkr}}{4\pi r}\;dz'=C_1e^{jkz}+C_2e^{-jkz}+\frac{1}{2\eta}\int_{-L/2}^{L/2}e^{-jk|z-z'|}\;E_z^i(z')\;dz'\;. \tag{5.34}$$

Note also that the two homogeneous terms in the above can also be written as

$$C_1 e^{jkz} + C_2 e^{-jkz} = D_1 \cos(kz) + D_2 \sin(kz) \, , \tag{5.35}$$

where D_1 and D_2 are complex. The form we use will depend on the symmetry of the problem.

5.3.1 Symmetric Problems

We first consider symmetric problems, such as a center-fed dipole antenna. Symmetry can reduce both the amount of computation and the number of unknown constants that must be determined. We first expand the left-hand side of (5.32) using N weighted basis functions, yielding

$$\sum_{n=1}^{N} a_n \int_{f_n} f_n(z') \frac{e^{-jkr}}{4\pi r} \, dz' \, . \tag{5.36}$$

Applying the Method of Moments and testing (5.32) using N testing functions f_m yields matrix elements Z_{mn} given by

$$Z_{mn} = \int_{f_m} f_m(z) \int_{f_n} f_n(z') \frac{e^{-jkr}}{4\pi r} \, dz' \, dz \, . \tag{5.37}$$

The choice of right-hand side depends on the symmetry of the problem being considered. Since we are feeding the antenna at its center, we expect that the induced current will be symmetric. Therefore, we will retain the right-hand side of (5.32) but rewrite the homogeneous terms following (5.35), yielding a right-hand side given by

$$D_1 \cos(kz) + D_2 \sin(kz) - \frac{j}{2\eta} \int_{-L/2}^{L/2} \sin(k|z - z'|) \, E_z^i(z') \, dz' \, . \tag{5.38}$$

As we expect the solution to be symmetric, we set D_2 in the above to zero. Applying the MOM to the right-hand side yields

$$D_1 \int_{f_m} f_m(z) \cos(kz) \, dz - \frac{j}{2\eta} \int_{f_m} f_m(z) \int_{-L/2}^{L/2} \sin(k|z - z'|) \, E_z^i(z') \, dz' \, dz \, , \tag{5.39}$$

which comprises a linear system of the form

$$\mathbf{Za} = D_1 \mathbf{s} + \mathbf{b} \, . \tag{5.40}$$

To obtain the solution vector **a**, we must determine the constant D_1. This can be done by enforcing the boundary conditions at the ends of the wire, which are

$$I_z(-L/2) = I_z(L/2) = 0 \, . \tag{5.41}$$

For the pulse discretization used here, we enforce the end condition by forcing the current represented by the first and last segments to zero [8]. This can be expressed vectorially as $\mathbf{u}^T \mathbf{a} = 0$, where $\mathbf{u}^T = [1, 0, \ldots, 0, 1]$. Solving (5.40) for **a** we obtain

$$\mathbf{a} = D_1 \mathbf{Z}^{-1} \mathbf{s} + \mathbf{Z}^{-1} \mathbf{b} \, , \tag{5.42}$$

and multiplying both sides by $\mathbf{u}^T$ results in

$$\mathbf{u}^T\mathbf{a} = D_1\mathbf{u}^T\mathbf{Z}^{-1}\mathbf{s} + \mathbf{u}^T\mathbf{Z}^{-1}\mathbf{b} = 0\,. \tag{5.43}$$

Finally, solving for D_1 yields

$$D_1 = -\frac{\mathbf{u}^T\mathbf{Z}^{-1}\mathbf{b}}{\mathbf{u}^T\mathbf{Z}^{-1}\mathbf{s}}\,. \tag{5.44}$$

The right-hand side vector can now be assembled from **s**, **b**, and D_1.

5.3.1.1 Solution Using Pulse Functions and Point Matching

For a simple implementation using pulse basis functions and point matching, we subdivide the wire into N equally spaced segments of length $\Delta_z = L/N$. The matrix elements of (5.37) are then

$$Z_{mn} = \int_{z_n-\Delta_z/2}^{z_n+\Delta_z/2} \frac{e^{-jkR}}{4\pi R}\,dz' \tag{5.45}$$

where the matching is done at the center of the testing segment ($z = z_m$), and $R = \sqrt{(z_m - z')^2 + a^2}$. Non-self terms can be evaluated directly from (5.45) using an M-point numerical quadrature.

5.3.1.1.1 Self Terms

When the source and testing segments overlap, we use a small-argument approximation to the Green's function to write

$$Z_{mm} = \int_{-\Delta_z/2}^{\Delta_z/2} \frac{e^{-jkR}}{4\pi R}\,dz' \approx \int_{-\Delta_z/2}^{\Delta_z/2} \frac{1-jkR}{4\pi R}\,dz' \tag{5.46}$$

which evaluates to [9] (200.01)

$$Z_{mm} = \frac{1}{4\pi}\log\left[\frac{\sqrt{1+4a^2/\Delta_z^2}+1}{\sqrt{1+4a^2/\Delta_z^2}-1}\right] - \frac{jk\Delta_z}{4\pi} \tag{5.47}$$

We assume that the approximation in (5.47) is valid when the segment is small compared to the wavelength.

5.3.1.1.2 Excitation

The elements of the right-hand side vectors **s** and **b** are

$$s_m = \cos(kz_m) \tag{5.48}$$

and

$$b_m = -\frac{j}{2\eta}\int_{-L/2}^{L/2} \sin\left(k|z_m - z'|\right)\,E_z^i(z')\,dz'\,, \tag{5.49}$$

where the impressed field has not yet been specified. For a unit-voltage ideal delta-gap excitation at the center of the wire, $E_z^i(z') = \delta(z')$, and (5.49) becomes

$$b_m = -\frac{j}{2\eta}\sin(k|z_m|)\ . \tag{5.50}$$

If we use the magnetic frill of (5.17), the convolution of (5.49) must be performed numerically for each z_m. Because of the fast drop-off in the frill amplitude, each integral should be carried out carefully to ensure its accuracy. In such cases, an adaptive quadrature technique is recommended.

5.3.2 Asymmetric Problems

When the feedpoint is not at the center of the antenna, or the wire is excited by an incident wave, we can no longer assume that the solution is symmetric. In this case, the elements of the system matrix remain the same as in (5.37), however we will use the more general right-hand side of (5.34). Testing the right-hand side with testing function f_m yields

$$\begin{aligned} &C_1\int_{f_m} f_m(z)e^{jkz}\,dz + C_2\int_{f_m} f_m(z)e^{-jkz}\,dz \\ &+\frac{1}{2\eta}\int_{f_m} f_m(z)\int_{-L/2}^{L/2} e^{-jk|z_m-z'|}\,E_z^i(z')\,dz'\,dz\ . \end{aligned} \tag{5.51}$$

The resulting matrix equation can be written as

$$\mathbf{Za} = C_1\mathbf{s}_1 + C_2\mathbf{s}_2 + \mathbf{b} = [\mathbf{s}_1\mathbf{s}_2][C_1C_2]^T + \mathbf{b} = \mathbf{SC} + \mathbf{b}\ , \tag{5.52}$$

where $\mathbf{S}$ is a $N \times 2$ matrix, and $\mathbf{C}$ is a 2×1 matrix. Solving for $\mathbf{a}$ then yields

$$\mathbf{a} = \mathbf{Z}^{-1}\big[\mathbf{SC} + \mathbf{b}\big] \tag{5.53}$$

To obtain $\mathbf{a}$, we must also solve for the constants C_1 and C_2, and as in the symmetric case, we will enforce the boundary conditions at the end of the wire. To do so, let us define the $2 \times N$ matrix

$$\mathbf{U} = \begin{bmatrix} \mathbf{u}_1^T \\ \mathbf{u}_2^T \end{bmatrix}, \tag{5.54}$$

where the row vectors $\mathbf{u}_1^T$ and $\mathbf{u}_2^T$ are

$$\mathbf{u}_1^T = [1, 0, \ldots, 0, 0] \tag{5.55}$$

and

$$\mathbf{u}_2^T = [0, 0, \ldots, 0, 1]\ . \tag{5.56}$$

Multiplying both sides of (5.53) by $\mathbf{U}$ yields

$$\mathbf{Ua} = \mathbf{UZ}^{-1}\big[\mathbf{SC} + \mathbf{b}\big] = 0\ , \tag{5.57}$$

and solving for $\mathbf{C}$ results in

$$\mathbf{C} = -\big[\mathbf{UZ}^{-1}\mathbf{S}\big]^{-1}\mathbf{UZ}^{-1}\mathbf{b}\ . \tag{5.58}$$

5.3.2.1 Solution Using Pulse Functions and Point Matching

The solution of the asymmetric Hallén's equation by point matching is similar to the symmetric case, as the system matrix elements remain the same. The only difference lies in the right-hand side vector elements.

5.3.2.1.1 Excitation

Using point matching, the right-hand side vector elements in (5.52) are

$$s_{1,m} = e^{jkz_m} \ , \tag{5.59}$$

$$s_{2,m} = e^{-jkz_m} \ , \tag{5.60}$$

and

$$b_m = \frac{1}{2\eta} \int_{-L/2}^{L/2} e^{-jk|z_m - z'|} \ E_z^i(z') \ dz' \ , \tag{5.61}$$

where we have not yet specified the incident field $E_z^i(z')$. For a unit-voltage ideal delta-gap source centered at z_c, $E_z^i(z') = \delta(z' - z_c)$, and (5.61) becomes

$$b_m = \frac{1}{2\eta} e^{-jk|z_m - z_c|} \ . \tag{5.62}$$

If instead the incident field comprises a magnetic frill or other incident field, (5.61) must be computed numerically for each z_m.

5.4 Pocklington's Equation

Pocklington's equation (5.13) can also be discretized directly with the Method of Moments. The main practical difference from Hallén's equation is that the differential operator acts on the Green's function, producing a more singular integrand. Expanding the current into a sum of N weighted basis functions, and testing with N testing functions, we obtain a linear system with matrix elements given by

$$Z_{mn} = \int_{f_m} f_m(z) \int_{f_n} f_n(z') \Big[1 + \frac{1}{k^2} \frac{\partial^2}{\partial z^2} \Big] \frac{e^{-jkr}}{r} \ dz' \ dz \tag{5.63}$$

and excitation vector elements given by

$$b_m = -j \frac{4\pi}{\omega\mu} \int_{f_m} f_m(z) \ E_z^i(z) \ dz \ . \tag{5.64}$$

5.4.1 Solution Using Pulse Functions and Point Matching

We again subdivide the wire into N equally spaced segments of length $\Delta_z = L/N$. With pulse basis functions and point matching at z_m, the first part of (5.63) is

$$\int_{z_n - \Delta_z/2}^{z_n + \Delta_z/2} \frac{e^{-jkR}}{R} \ dz' \ , \tag{5.65}$$

where

$$R = \sqrt{(z_m - z')^2 + a^2}\,. \tag{5.66}$$

We note that (5.65) has the same form as (5.45), and can be computed the same way. The second part of (5.63) can be written as

$$\frac{1}{k^2}\int_{f_m} f_m(z)\int_{f_n} f_n(z')\frac{\partial^2}{\partial z^2}\frac{e^{-jkR}}{R}\,dz'\,dz\,. \tag{5.67}$$

Evaluating the first partial derivative in the integrand yields

$$\frac{\partial}{\partial z}\frac{e^{-jkR}}{R} = -(z-z')\frac{1+jkR}{R^3}e^{-jkR}\,, \tag{5.68}$$

and inserting the above into (5.67) yields

$$\frac{1}{k^2}\int_{f_m} f_m(z)\int_{f_n} f_n(z')\frac{\partial}{\partial z}\left[-(z-z')\frac{1+jkR}{R^3}e^{-jkR}\right]dz'dz\,. \tag{5.69}$$

We note that in (5.66) and (5.69), z and z' always appear together as $(z - z')$. Thus, we can replace $\partial/\partial z$ with $-\partial/\partial z'$, and using pulse basis functions and point matching at $z = z_m$, the above evaluates to

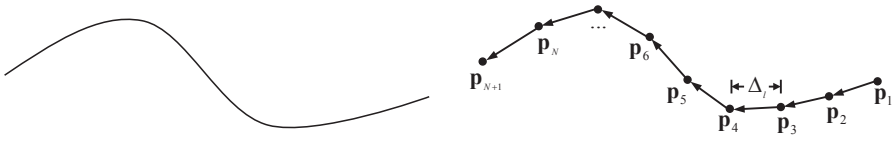
$$\frac{1}{k^2}\left[(z_m - z')\frac{1+jkR}{R^3}e^{-jkR}\right]\Bigg|_{z'=z_n-\Delta_z/2}^{z'=z_n+\Delta_z/2}\,, \tag{5.70}$$

which allows us to write the matrix elements as

$$Z_{mn} = \int_{z_n-\Delta_z/2}^{z_n+\Delta_z/2}\frac{e^{-jkR}}{R}\,dz' + \frac{1}{k^2}\left[(z_m-z')\frac{1+jkR}{R^3}e^{-jkR}\right]\Bigg|_{z'=z_n-\Delta_z/2}^{z'=z_n+\Delta_z/2}\,. \tag{5.71}$$

The second term is analytic and can be used as-is in computing each matrix element. Because of the strongly singular $1/R^3$ term, we will find that our results converge less quickly than those obtained using Hallén's equation for the same problem. The corresponding right-hand side vector elements are

$$b_m = -j\frac{4\pi}{\omega\mu}E_z^i(z_m)\,. \tag{5.72}$$



(a) Curved Thin Wire (b) Discretization

Figure 5.3: Curved Thin Wire Discretization

5.5 Thin Wires of Arbitrary Shape

The formulations considered thus far treated wires that are perfectly straight. However, realistic wire antennas have curves, bends, and junctions. In this section, we develop a thin-wire EFIE formulation to handle this type of geometry.

5.5.1 Method of Moments Discretization

Consider a curved thin wire, illustrated in Figure 5.3a. We subdivide the curve into N segments with $N + 1$ endpoints as shown in Figure 5.3b. The segments need not be equal in length, but they should be short enough to represent the local curvature accurately and to provide adequate spatial resolution at the operating wavelength. The tangent vector on the curve is now a piecewise continuous function, as is illustrated with the arrows. As the wire supports only electric currents, we will enforce the EFIE (3.181). The filamentary current $\mathbf{J}(\mathbf{r})$ is expanded using electric basis functions $\mathbf{f}(\mathbf{r})$ whose vector components are tangent to the segment(s) on which it resides. Testing the EFIE with these same functions yields the matrix elements (3.188) for the thin wire case, which are

$$Z_{mn}^{EJ} = \int_{\mathbf{f}_m} \mathbf{f}_m(\mathbf{r}) \cdot \int_{\mathbf{f}_n} \mathbf{f}_n(\mathbf{r}') \, \frac{e^{-jkr}}{r} \, d\mathbf{r}' \, d\mathbf{r} \\ -\frac{1}{k^2} \int_{\mathbf{f}_m} \nabla \cdot \mathbf{f}_m(\mathbf{r}) \int_{\mathbf{f}_n} \nabla' \cdot \mathbf{f}_n(\mathbf{r}') \, \frac{e^{-jkr}}{r} \, d\mathbf{r}' \, d\mathbf{r} \, , \tag{5.73}$$

where $r = |\mathbf{r} - \mathbf{r}'|$, and we have re-distributed the differential operators following (3.207). The first integral comprises the "vector" part of the matrix element, and the second the "scalar" part. The right-hand side vector elements (3.194) are

$$V_m^E = -j\frac{4\pi}{\omega\mu} \int_{\mathbf{f}_m} \mathbf{f}_m(\mathbf{r}) \cdot \mathbf{E}^i(\mathbf{r}) \, d\mathbf{r} \, . \tag{5.74}$$

We refer to the approach in this section as a thin-wire EFIE. Similar approaches are found in the literature.

5.5.2 Solution Using Triangle Basis and Testing Functions

We will use triangle functions to solve the thin-wire EFIE. As the current must go to zero on the ends of the wire, we assign triangle functions everywhere except at the wire

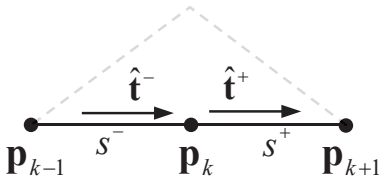


Figure 5.4: Vector Triangle Function Orientation

endpoints. Also, as the basis functions have vector components, they must be oriented properly. Consider a triangle function which has support on segments s^+ and s^- whose endpoints comprise $(\mathbf{p}_{k-1}, \mathbf{p}_k, \mathbf{p}_{k+1})$, as shown in Figure 5.4. The vector components are $\mathbf{t}^+$ on s^+, and $\hat{\mathbf{t}}^-$ on s^-. Although the vector orientations are shown from right to left, reversing both orientations is equally valid. The important requirement is that the basis function be continuous in the sense of current flow at $\mathbf{p}_k$, consistent with Kirchhoff's current law.

Note that on a segment, it is convenient to write the basis or testing functions as $\mathbf{f}(\mathbf{r}) = f(\mathbf{r})\hat{\mathbf{t}}$, where $f(\mathbf{r})$ is the scalar triangle function. We will use this notation in the following sections.

5.5.2.1 Regular Terms

For segments that do not overlap, the matrix elements (5.73) are computed using an M-point numerical quadrature rule, yielding

$$Z_{mn}^{EJ} = \hat{\mathbf{t}}_m \cdot \hat{\mathbf{t}}_n \sum_{p=1}^{M} w_p(\mathbf{r}_p) f_m(\mathbf{r}_p) \sum_{q=1}^{M} w_q(\mathbf{r}_q) f_n(\mathbf{r}_q) \frac{e^{-jkR_{pq}}}{R_{pq}} \pm \frac{1}{k^2 \Delta_p \Delta_q} \sum_{p=1}^{M} w_p(\mathbf{r}_p) \sum_{q=1}^{M} w_q(\mathbf{r}_q) \frac{e^{-jkR_{pq}}}{R_{pq}} \,. \tag{5.75}$$

where $\mathbf{r}_p$ and $\mathbf{r}_q$ are quadrature points on each segment, Δ_p and Δ_q are the divergence of the testing and source triangle at $\mathbf{r}_p$ and $\mathbf{r}_q$, respectively, and

$$R_{pq} = |\mathbf{r}_p - \mathbf{r}'_q| \,. \tag{5.76}$$

The first term in (5.75) comprises the vector part of the integral, and the second is the scalar part of the integral. Because the vector component and divergence of each triangle function is constant on a segment, those components have been moved outside the sums. For a triangle function that flows into or out of its anchor point on a segment of length Δ_l, its divergence is $1/\Delta_l$ or $-1/\Delta_l$ on that segment, respectively. Thus, the sign of the second term depends on the orientation of the triangle functions on the source and testing segments. In practical implementations, it is more efficient to compute the matrix elements by looping over pairs of segments instead of pairs of basis and testing functions.

5.5.2.2 Self Terms

When segments overlap, the Green's function is singular and the integrals in (5.73) evaluated carefully. To begin, first we rewrite (5.73) as

$$Z_{mn}^{EJ} = \int_0^{\Delta_l} f_m(x) \int_0^{\Delta_l} f_n(x') \frac{e^{-jkr}}{r}\, dx'\, dx \\ \pm \frac{1}{k^2 \Delta_l \Delta_l} \int_0^{\Delta_l} \int_0^{\Delta_l} \frac{e^{-jkr}}{r}\, dx'\, dx\ , \tag{5.77}$$

where $r = \sqrt{(x-x')^2 + a^2}$, and Δ_l is the length of the segment. In this case, we will evaluate the outermost integrals umerically and the innermost integrals analytically. The two innermost integrals are

$$I_1(x) = \int_0^{\Delta_l} f_n(x') \frac{e^{-jkr}}{r}\, dx'\ , \quad I_2(x) = \int_0^{\Delta_l} \frac{e^{-jkr}}{r}\, dx'\ . \tag{5.78}$$

On the segment, there are two half-triangle functions, $f_1(x) = x'/\Delta_l$ (with positive slope), and $f_2(x') = 1 - x'/\Delta_l$ (with negative slope). Therefore, computing $I_1(x)$ for each requires evaluating integrals of the form

$$I_{s,1}(x) = \frac{1}{\Delta_l} \int_0^{\Delta_l} x' \frac{e^{-jkr}}{r}\, dx'\ , \tag{5.79}$$

and

$$I_{s,2}(x) = \int_0^{\Delta_l} \left[1 - \frac{x'}{\Delta_l}\right] \frac{e^{-jkr}}{r} = I_2 - I_{s,1}\ . \tag{5.80}$$

First, we compute $I_2(x)$. Using the small-argument approximation to the Green's function

$$\frac{e^{-jkr}}{r} = \frac{\cos(kr) - j\sin(kr)}{r} \approx \frac{1}{r} - jk \qquad r \to 0\ , \tag{5.81}$$

we can write

$$I_2(x) = \int_0^{\Delta_l} \left[\frac{1}{r} - jk\right]\, dx' = \int_0^{\Delta_l} \frac{1}{\sqrt{(x-x')^2 + a^2}}\, dx' - jk\Delta_l\ , \tag{5.82}$$

which evaluates to [10]

$$I_2(x) = \log\left[\frac{x + \sqrt{a^2 + x^2}}{x - \Delta_l + \sqrt{a^2 + (x-\Delta_l)^2}}\right] - jk\Delta_l\ . \tag{5.83}$$

We next write $I_{s,1}$ as

$$I_{s,1}(x) = \frac{1}{\Delta_l} \int_0^{\Delta_l} x' \left[\frac{1}{r} - jk\right]\, dx' = \frac{1}{\Delta_l} \int_0^{\Delta_l} \frac{x'}{\sqrt{(x-x')^2 + a^2}}\, dx' - jk\frac{\Delta_l}{2}\ , \tag{5.84}$$

which evaluates to [10]

$$I_{s,1}(x) = \frac{1}{\Delta_l}\sqrt{a^2+(x-\Delta_l)^2} - \frac{1}{\Delta_l}\sqrt{a^2+x^2} + \frac{x}{\Delta_l}\log\left[\frac{x+\sqrt{a^2+x^2}}{x-\Delta_l+\sqrt{a^2+(x-\Delta_l)^2}}\right] - \frac{jk\Delta_l}{2} . \tag{5.85}$$

The self-term contributions to (5.73) can then be obtained via numerical quadrature as

$$\sum_{p=1}^{M} w_p(x_p) f_m(x_p) I_1(x_p) \pm \frac{1}{k^2\Delta_l\Delta_l}\sum_{p=1}^{M} w_p(x_p) I_2(x_p) , \tag{5.86}$$

where $I_1(x_p)$ becomes either $I_{s,1}(x_p)$ or $I_{s,2}(x_p)$ depending on the slope of the testing function.

5.5.3 Solution Using Sinusoidal Basis and Testing Functions

The sinusoidal basis solution follows the same overall procedure as the triangle basis solution, where the regular terms are given by (5.75). The main difference lies in the divergence of the basis functions, and the self-term evaluation, where we again evaluate the outer integrals numerically, and the inner integrals analytically.

5.5.3.1 Self Terms

To calculate the first term on the right in (5.73), consider the innermost integral with a sinusoid function of positive slope, given by

$$S_1(x_p) = \frac{1}{\sin(k\Delta_l)}\int_0^{\Delta_l} \sin(kx')\frac{e^{-jkr}}{r}\,dx' . \tag{5.87}$$

where $r = \sqrt{(x_p-x')^2+a^2}$. Again using the small-argument approximation to the Green's function this becomes

$$\int_0^{\Delta_l} \sin(kx')\frac{e^{-jkr}}{r}\,dx' \approx \int_0^{\Delta_l} \sin(kx')\left[\frac{1-jkr}{r}\right]dx' , \tag{5.88}$$

which is

$$\int_0^{\Delta_l} \sin(kx')\left[\frac{1-jkr}{r}\right]dx' = \int_0^{\Delta_l}\frac{\sin(kx')}{r}\,dx' + j\big[\cos(k\Delta_l)-1\big] . \tag{5.89}$$

The first term on the right is not tractable in its present form, so we will approximate the sine by its third-order polynomial approximation. This yields

$$\int_0^{\Delta_l}\frac{\sin(kx')}{r}\,dx' \approx \int_0^{\Delta_l}\frac{kx'-(kx')^3/6}{\sqrt{(x_p-x')^2+a^2}}\,dx' . \tag{5.90}$$

Which evaluates to [10]

$$S_1(x_p) = C\frac{kx_p}{12}\left(\Big[-3a^2k^2 + 2x_p^2k^2 - 12\Big]\log\left[x_p - x' + \sqrt{a^2 + (x_p - x')^2}\right]\right.$$
$$-\frac{k}{36}\Big[-4a^2k^2 + k^2\big(11x_p^2 + 5x'x_p - 2(x')^2\big) - 36\Big]$$
$$\left.\sqrt{a^2 + (x_p - x')^2}\right)\Bigg|_0^{\Delta_l} + jC\big[\cos(k\Delta_l) - 1\big]\,, \tag{5.91}$$

where $C = 1/\sin(k\Delta_l)$. Although this expression is lengthy, it can be evaluated numerically in a straightforward manner.

We compute the second term on the right of (5.73) the same way. Under the small-argument approximation to the Green's function, the innermost integral in this case is

$$S_2(x_p) = \frac{k}{\sin(k\Delta_l)}\int_0^{\Delta_l}\frac{\cos(kx')}{r}\,dx' - jk\,. \tag{5.92}$$

We approximate the cosine by the second-order approximation, yielding the integral

$$\int_0^{\Delta_l}\frac{\cos(kx')}{r}\,dx' \approx \int_0^{\Delta_l}\frac{1 - (kx')^2/2}{\sqrt{(x_p - x')^2 + a^2}}\,dx'\,. \tag{5.93}$$

The above evaluates to [10]

$$S_2(x_p) = -C\frac{k}{4}\left(k^2\big[3x_p + x'\big]\sqrt{a^2 + (x_p - x')^2} + (a^2k^2 - 2x_p^2k^2 + 4)\right.$$
$$\left.\log\left[x_p - x' + \sqrt{a^2 + (x_p - x')^2}\right]\right)\Bigg|_0^{\Delta_l} - jk\,. \tag{5.94}$$

The self-term contributions to (5.73) can then be obtained via numerical quadrature as

$$\sum_{p=1}^{M} w_p(x_p)s_m(x_p)S_1(x_p) - \frac{1}{k^2}\sum_{p=1}^{M} w_p(x_p)s_m'(x_p)S_2(x_p)\,, \tag{5.95}$$

where $s_m(x)$ is the sinusoidal testing function. Although we considered only the sinusoid function having positive slope, these results can be used to compute all the self terms by using the correct testing function $s_m(x)$ in a symmetric fashion.

5.5.4 Lumped and Distributed Impedances

In some cases it may be necessary to modify the impedance characteristics of an antenna by loading it at one or more points. Feedpoint matching is one of the most common adjustments, and is done by placing an impedance in parallel at the feedpoint, or by inserting coils or capacitors at one or more points along the wire. To model these

lumped impedances in the thin wire EFIE, we must take into account the boundary conditions on the segments where the loads exist. For a lumped impedance Z_l on a segment of length Δ_l, the boundary condition on this segment is

$$E^i_{tan} + E^s_{tan} = E_{load} = \frac{V_l}{\Delta_l} = \frac{Z_l I_l}{\Delta_l} \,. \tag{5.96}$$

The right-hand side of the EFIE now becomes

$$\frac{Z_l I_l}{\Delta_l} - E^i_{tan} \,, \tag{5.97}$$

where I_l is the current associated with the loaded segment. In a discretized model, that current may be represented by one or more basis functions. If we use triangle functions in the thin wire EFIE, the testing operation with the basis function f_m creates a "self term" on the right-hand side of the form

$$b'_m = \frac{Z_l}{2} \,, \tag{5.98}$$

which can then be moved to the left-hand side and subtracted from the diagonal element Z^{EJ}_{mm}. Any basis function having support on this segment will have its self term modified in this manner.

5.6 Examples

In this section we consider several thin wire antenna problems. We first compare the relative performance of the Hallén, Pocklington, and thin-wire EFIE models for a straight wire antenna. We will then use the thin-wire EFIE to model a half-wavelength dipole, circular loop, folded dipole, two-wire transmission line, and finally, a multi-element Yagi antenna.

5.6.1 Comparison of Thin Wire Models

For this comparison, we compute the input impedance and induced current distribution on center-fed dipole antennas. We assess each formulation by examining convergence as the number of wire segments is increased. We use a delta-gap source of 1 V and an odd number of wire segments so the delta-gap voltage source is exactly at the center of the antenna. For numerical integration, a 5-point Gaussian quadrature is used on each segment. Each dipole has a radius of $5 \times 10^{-4}\lambda$.

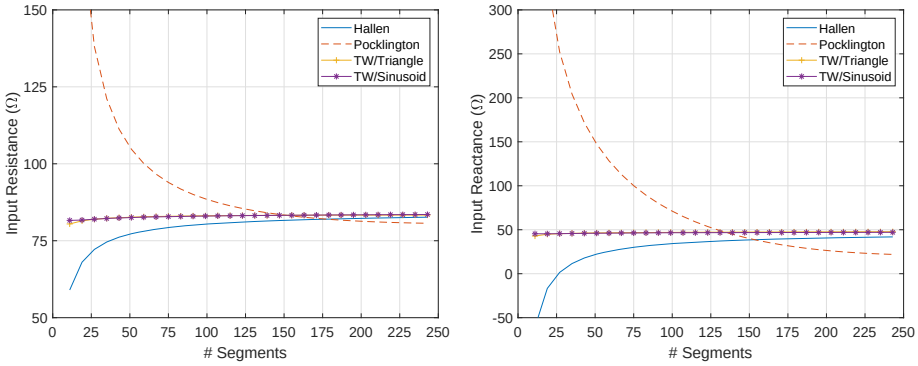
5.6.1.1 Input Impedance

First, we will compare the convergence of the input impedance versus the number of wire segments used. We first consider a dipole of length $\lambda/2$, where the resistance and reactance are plotted in Figures 5.5a and 5.5b, respectively. The thin-wire EFIE results converge rapidly, whereas the Hallén and Pocklington results approach similar values more slowly. This is not surprising, as triangle and sinusoidal functions are better at modeling the current distribution than pulses, and they enforce the boundary conditions more accurately than with point matching. Similar comparisons for a $3\lambda/2$ dipole are made in Figures 5.6a and 5.6b, respectively. The results from the thin wire EFIE models again converge quickly, whereas Pocklington's Equation performs quite poorly at low segment counts. This illustrates the limitations of pulse basis functions and point matching in this problem, combined with the numerical sensitivity associated with the $1/R^3$ behavior of the Pocklington kernel.

We next set the number of segments per wavelength to 25, and vary the length of the dipole from 0.1 to 3λ. The results are shown in Figure 5.7. The thin-wire EFIE results agree well at almost every data point, suggesting that triangles and sinusoids have similar performance characteristics for thin wire problems. The impedances obtained from Hallén's and Pocklington's Equation do not agree very well at this level of discretization, as expected.

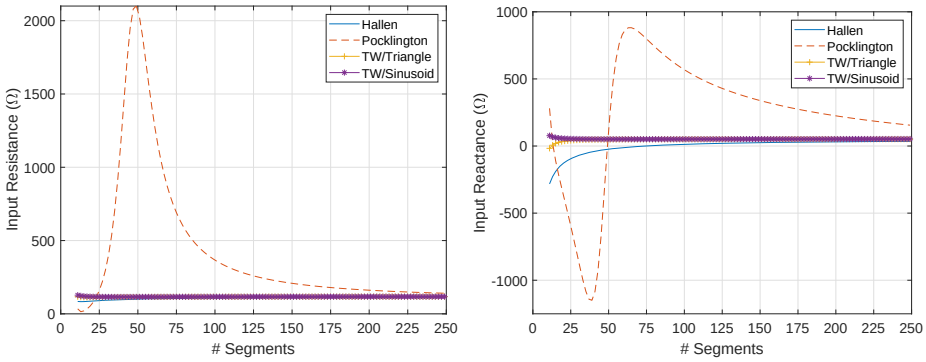
5.6.1.2 Induced Current Distribution

We next compare the currents induced on a center-fed dipole computed using each thin wire model. For the comparison, we plot the current at the center of each wire segment. Note that the solution via Hallén's equation will yield exactly zero current in the first and last segments, as this was enforced explicitly. In Figures 5.8a and 5.8b are shown the currents induced on a $\lambda/2$ dipole computed using 31 and 81 wire segments, respectively. The thin-wire EFIE models show almost no change between the two



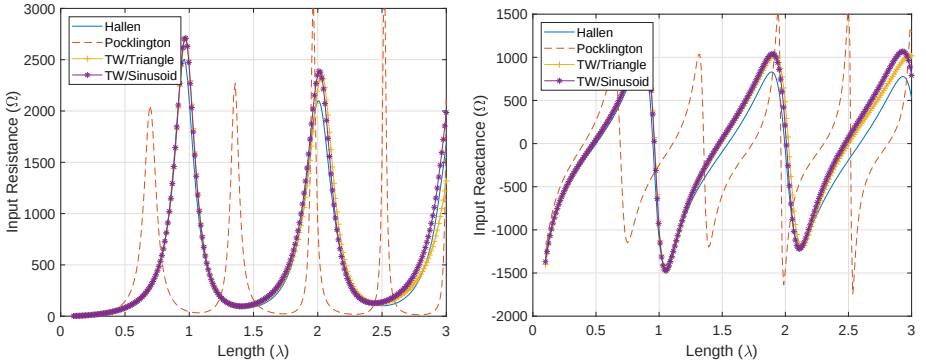
(a) Input Resistance (b) Input Reactance

Figure 5.5: Input Impedance of a $\lambda/2$ Dipole



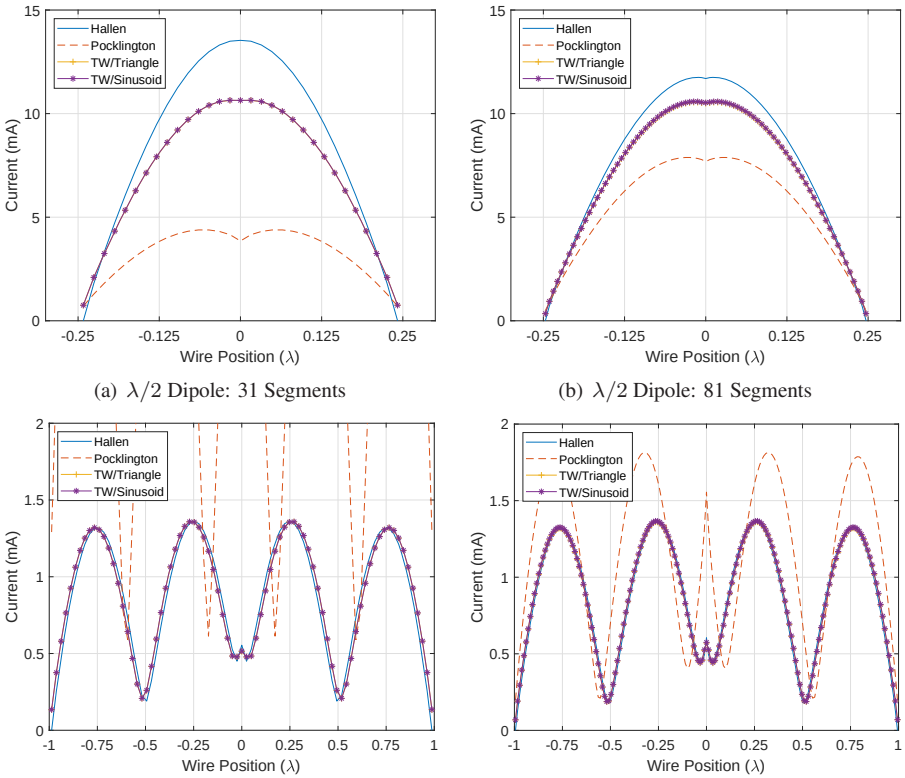
(a) Input Resistance (b) Input Reactance

Figure 5.6: Input Impedance of a $3\lambda/2$ Dipole



(a) Input Resistance (b) Input Reactance

Figure 5.7: Input Impedance versus Dipole Length



(a) $\lambda/2$ Dipole: 31 Segments

(b) $\lambda/2$ Dipole: 81 Segments

(c) 2λ Dipole: 81 Segments

(d) 2λ Dipole: 181 Segments

Figure 5.8: Induced Currents on $\lambda/2$ and 2λ Dipoles

figures indicating excellent convergence, whereas the currents obtained from Hallén's and Pocklington's equation vary significantly. Results for a 2λ dipole are shown in Figures 5.8c and 5.8d for 81 and 181 wire segments, respectively. Hallén's equation does somewhat better at the lower segment count than does Pocklington's equation, though they are both fairly good at the higher count. The convergence of the thin-wire EFIE models is again excellent.

5.6.2 Half-Wavelength Dipole

It is known that a center-fed dipole in free space has its first resonance at a length just under $\lambda/2$. Using the thin-wire EFIE, a delta-gap excitation of 1 V and 35 wire segments, we find by iteration that a dipole of radius $10^{-4}\lambda$ and length approximately 0.475λ has a purely resistive input impedance of 72 Ω. This antenna could be fed directly with a $50\ \Omega$ or $75\ \Omega$ coaxial cable (for example, RG-58 or RG-59, respectively) with a reasonably low standing wave ratio (SWR).

We now set the feedpoint at the origin and align the antenna with the z axis. Using the induced current from the delta-gap source, we compute the near field in a $20\lambda \times 20\lambda$ region of the xz plane using (3.108). The real part of the electric field (in V/m) is plotted in Figure 5.9a. We note that the extent of the near field region is small, and the amplitude decays quickly along the z axis.

Next we compare the computed field pattern to that of an ideal dipole from antenna theory. We recall that the radiated electric field of an infinitesimal, $\hat{\mathbf{z}}$-oriented electric current has $\hat{\mathbf{r}}$ and $\hat{\boldsymbol{\theta}}$ components given by

$$E_r(r,\theta) = -\frac{k^2\eta I \Delta_l}{2\pi}\Big[\frac{1}{(jkr)^2} + \frac{1}{(jkr)^3}\Big]\cos\theta\, e^{-jkr} \tag{5.99}$$

and

$$E_\theta(r,\theta) = -\frac{k^2\eta I \Delta_l}{2\pi}\Big[\frac{1}{jkr} + \frac{1}{(jkr)^2} + \frac{1}{(jkr)^3}\Big]\sin\theta\, e^{-jkr}\ , \tag{5.100}$$

where I is the current amplitude and Δ_l is its length, where $\Delta_l \ll \lambda$. If we know $I(z)$, we can then integrate over the length of the dipole to determine the total near field. For the dipole, we will use an ideal sinusoidal distribution model for current, where

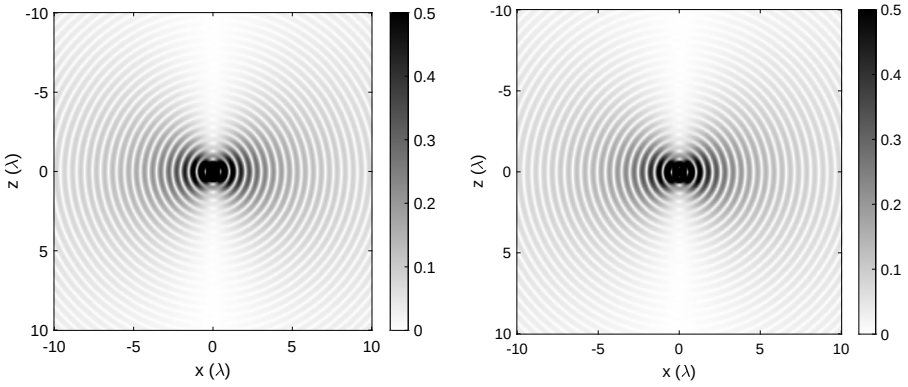
$$I(z) = I_0 \sin\big[k(L/2 - z)\big]\ . \tag{5.101}$$

For I_0, we use the numerically computed feedpoint current, and $L = 0.475\lambda$ as before. In Figure 5.9b is plotted the real part of the near electric field (in V/m) in the same region, computed using (5.99–5.101). To the eye, the results are nearly indistinguishable. In Figure 5.10a, we compare the computed currents to those of (5.101), where the currents have slightly different amplitude envelopes but are otherwise very similar.

Finally, we sample the computed near field in the xz plane at a fixed distance of 10λ from the antenna for $0 \le \theta \le 2\pi$. To this, we compare the normalized far electric field of an ideal $\lambda/2$ dipole, which is [11]

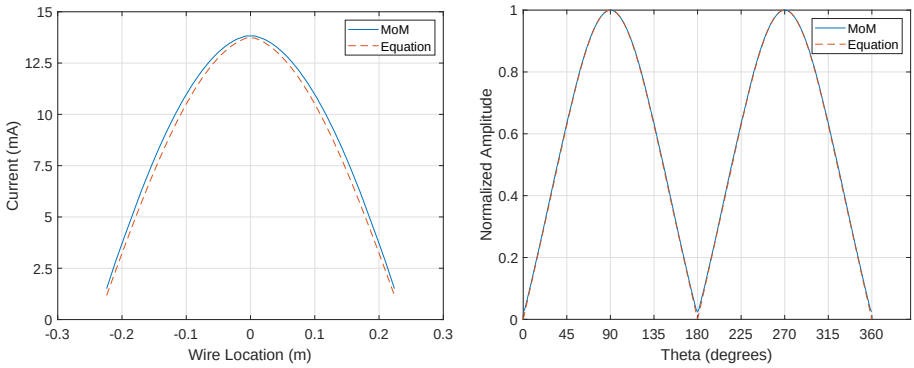
$$E_\theta(\theta) = \frac{\cos\big(\frac{\pi}{2}\cos\theta\big)}{\sin\theta}\ . \tag{5.102}$$

The normalized amplitudes are compared in Figure 5.10b, where the results are again very similar.



(a) MoM (b) Equation

Figure 5.9: Near Field ($|\operatorname{Re}(\mathbf{E})|$, V/m) of a 0.475λ Dipole



(a) Current Amplitudes (b) Normalized Far Field Pattern

Figure 5.10: Current Amplitudes and Far Field Patterns of the 0.475λ Dipole

5.6.3 Circular Loop Antenna

We next consider the input impedance and radiation pattern of a circular loop antenna located in the xy plane. For a wire of radius $10^{-4}\lambda$, we vary the circumference of the loop up to 2.5λ. At each step, we use approximately 10 segments per wavelength, with no fewer than 35 segments for the smaller loops. This ensures that the model retains the shape of a circle at the lowest frequency. The feedpoint of the antenna is placed at the point where the $+x$ axis intersects the loop ($y = 0$), and a delta-gap excitation is used. The real and imaginary parts of the input impedance are shown in Figure 5.11. For lengths less than 0.5λ, we see that the loop has a high inductance and virtually no radiation resistance. At approximately $\lambda/2$, the loop becomes an open circuit. We find first and second resonances at approximately 1.03λ and 2.05λ, where the resistance is approximately 140 Ω and 182 Ω, respectively.

Using the induced current on the 2.05λ loop antenna, we compute the near field in

a $20\lambda \times 20\lambda$ region of the xy plane using (3.108). The real part of the electric field (in V/m) is plotted in Figure 5.12a. The corresponding normalized field amplitude at a distance d of 10λ is shown versus ϕ in Figure 5.12b. Four nulls are visible, with a slight asymmetry in the pattern. Similar plots in the xz plane are shown in Figures 5.13a and 5.13b, where the pattern is significantly different. To better visualize the overall radiation pattern in three dimensions, we compute the normalized radiated field for all θ and ϕ on the unit sphere, again at a distance of 10λ, as shown in Figure 5.14.

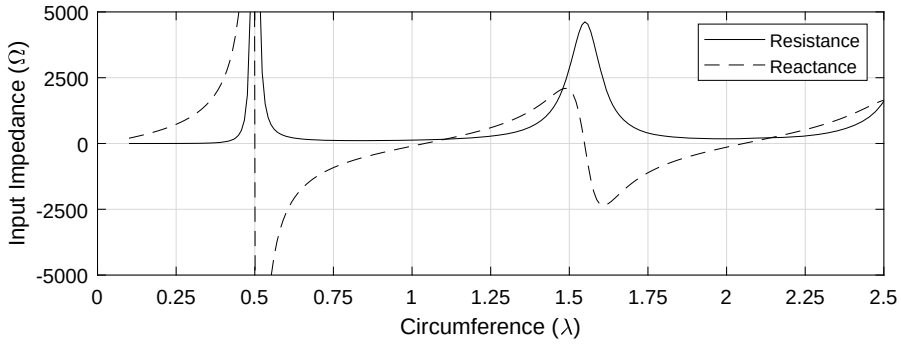
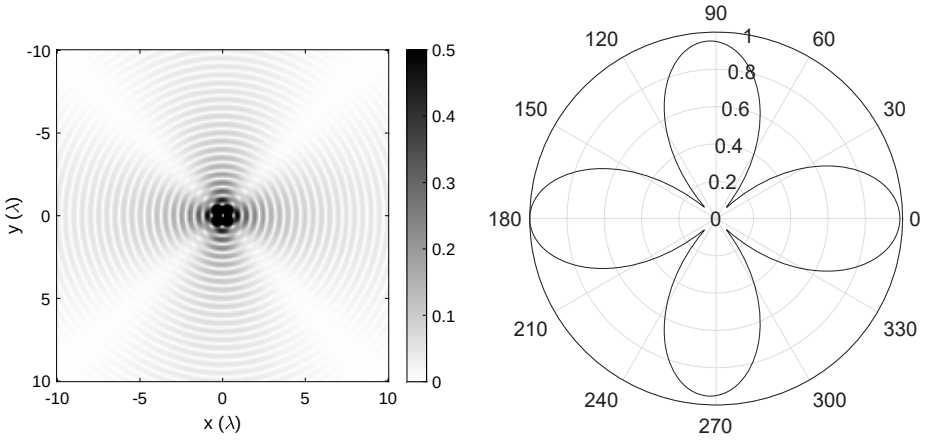
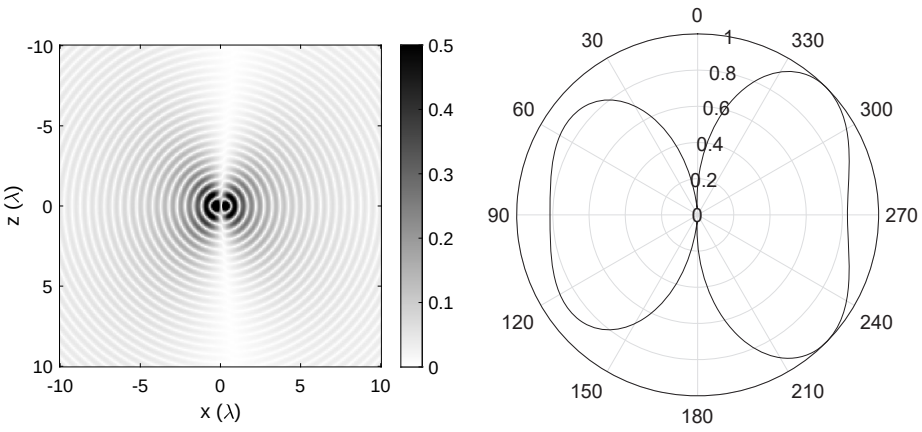


Figure 5.11: Circular Loop Input Impedance



(a) Near Field ($|\,\mathrm{Re}(\mathbf{E})|$, V/m) (b) Field Amplitude ($d = 10\lambda$)

Figure 5.12: Radiated Field of the Circular Loop (xy plane)



(a) Near Field ($|\,\mathrm{Re}(\mathbf{E})|$, V/m) (b) Field Amplitude ($d = 10\lambda$)

Figure 5.13: Radiated Field of the Circular Loop (xz plane)

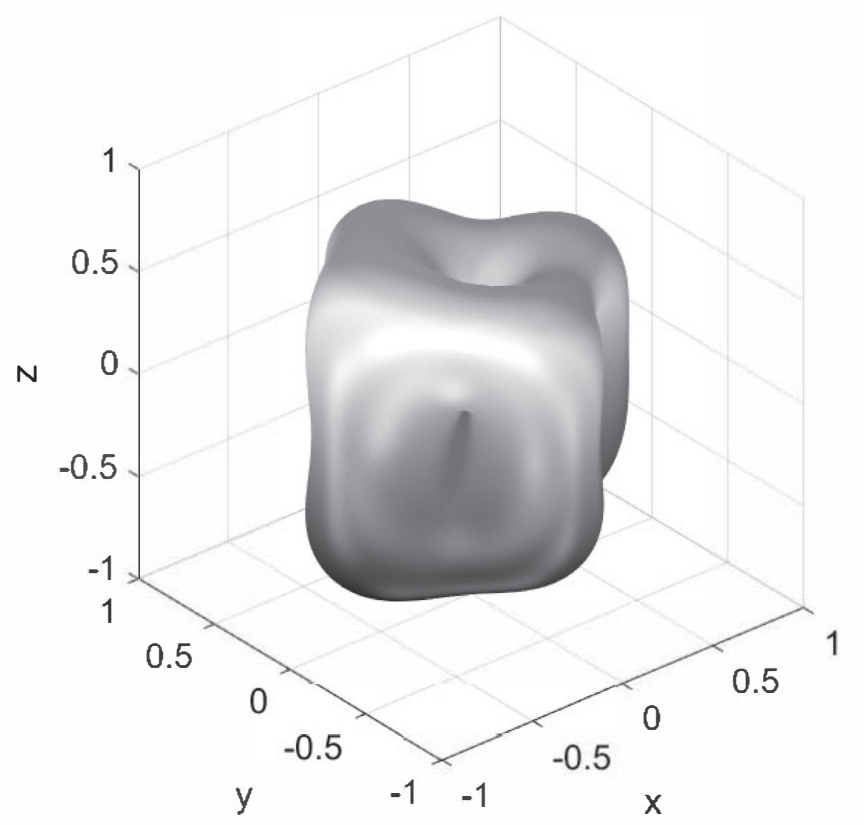
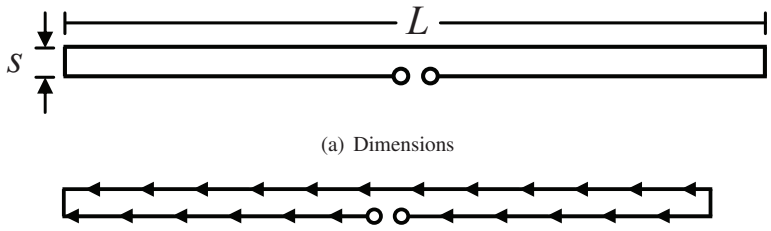


Figure 5.14: 3D Radiated Field Pattern of the Circular Loop



(a) Dimensions

(b) Nominal Current Distribution at $\lambda/2$

Figure 5.15: Folded Dipole Antenna

5.6.4 Folded Dipole Antenna

The folded dipole is an antenna commonly used in HF and VHF systems. It gets this name as it is a dipole that is essentially "folded over on itself," comprising a square loop that is very short in one dimension. This is illustrated in Figure 5.15a, where the loop has a length of L and width of s, and a feedpoint in the center of one of the long sides. At DC, this antenna is a short circuit, but as its length increases the current changes, and when $L \approx \lambda/2$ it assumes the distribution of Figure 5.15b. In this case, the currents on the secondary side of the loop take on the same magnitude and phase as those on the primary side. As s is very small, the far radiated field remains much the same, however the current is divided evenly between the two halves. Therefore, the input impedance of the folded dipole is four times that of an ordinary dipole at its first resonance, or approximately $288\ \Omega$. Folded dipoles are often used because of this property, as they can be matched to open-wire feed lines having a higher impedance than coaxial cable (which is typically 50Ω).

In Figure 5.16 is plotted the input impedance of a folded dipole for $L \leq 2\lambda$, where $s = L/20$ and the radius of the wire is 10^{-4}. The dipole is placed in the xz plane, with the feedpoint at the origin. We use 30 segments for each long conductor and 5 segments for the short ends, and a delta-gap source is used. We observe that when the dipole is electrically small it behaves like the circular loop, having virtually no radiation resistance, and at a length of about 0.3λ it becomes an open circuit. The first resonance occurs at a length of about 0.46λ where the input resistance is $284\ \Omega$, close to the expected value. The next resonance occurs at a length of about 0.95λ, however the antenna has almost zero radiation resistance. This is because the currents on the primary and secondary sides are now out of phase, and there is very little radiated field. The next resonance is at a length of about 1.4λ, where the currents are again in phase, and the input resistance is about 400Ω.

We next place the 0.46λ folded dipole at the origin, oriented in the xz plane. Using a delta-gap source of 1 V, we then compute the radiated near field in the xz plane, where the real part of the electric field (in V/m) is plotted in Figure 5.17. It is similar, but not identical, to the near field pattern of the 0.475λ dipole observed in Figure 5.9a.

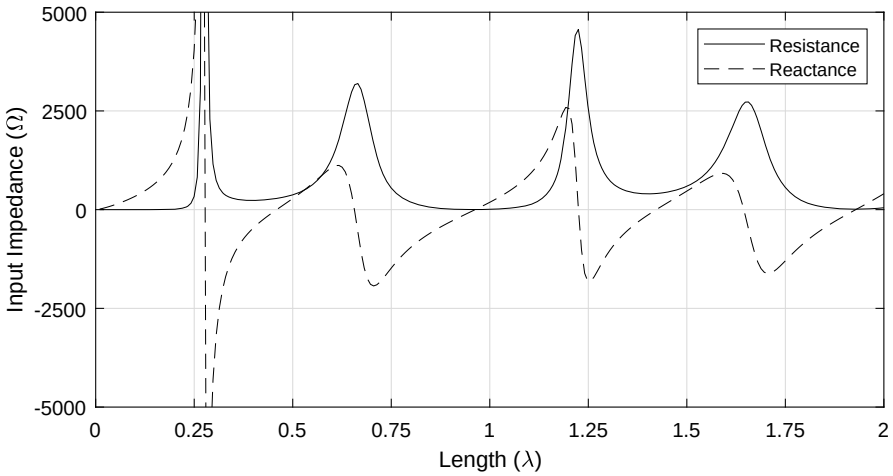


Figure 5.16: Folded Dipole Input Impedance

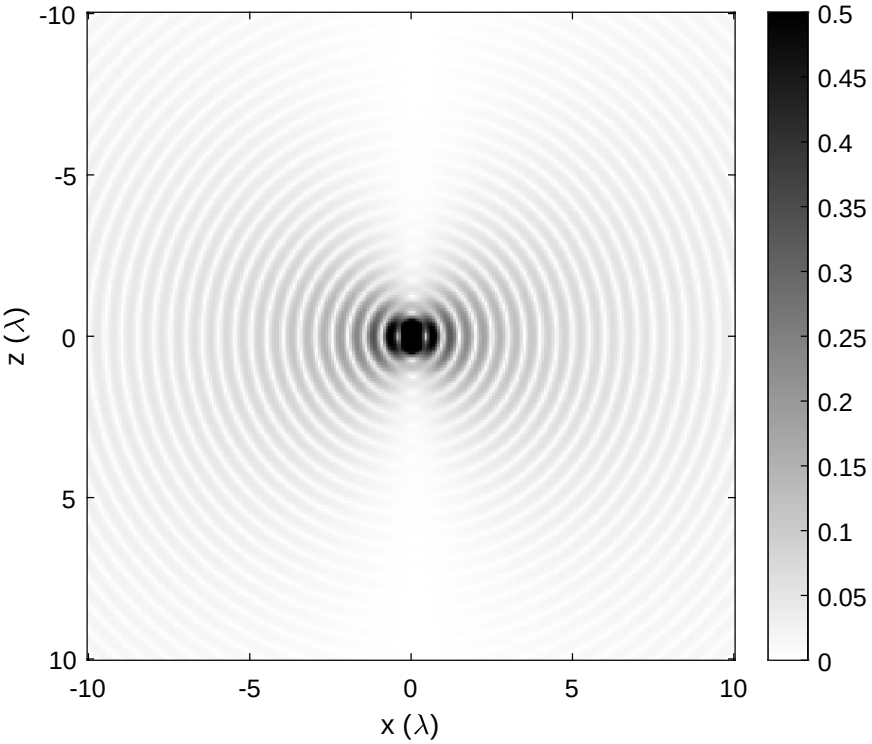


Figure 5.17: Near Field ($|\,\mathrm{Re}(\mathbf{E})|$, V/m) of the Folded Dipole (xz plane)

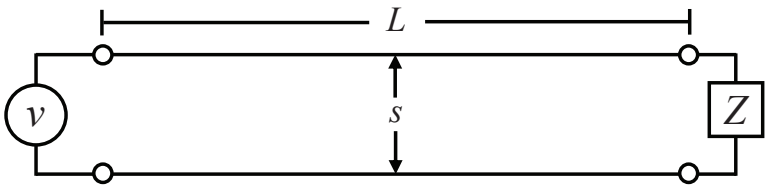


Figure 5.18: Two-Wire Transmission Line

5.6.5 Two-Wire Transmission Line

As transmission lines are implicit in virtually all antenna problems, we will next examine the behavior of a common two-wire transmission line illustrated in Figure 5.18, Two-wire line (also called "ladder line") is typically constructed of two copper wires, which are held a precise distance apart by a vinyl sheath or flat plastic ribbon. In two-wire line, the ribbon often has rectangular holes cut into it at regular intervals for weight reduction, giving it the appearance of a ladder. For the purposes of simulation, we will ignore the presence of a sheath or ribbon, and treat the two-wire line in an identical manner to the folded dipole of Section 5.6.4, except that the feedpoint and load are placed at the short ends. We will analyze a two-wire line 2.5 meters long, constructed of wires 1 mm in radius having a separation distance of 3 cm. We use 31 segments for the longer main wires and 5 segments for the ends.

Our first task is to determine the characteristic impedance of the line. The theoretical value for a two-wire line is obtained from transmission line theory [8] and is

$$Z_0 = \sqrt{L_0/C_0} \tag{5.103}$$

where L_0 is the inductance per unit length

$$L_0 = \frac{\mu_0}{\pi} \cosh^{-1}\left(\frac{s}{2a}\right), \tag{5.104}$$

and C_0 is the capacitance per unit length

$$C_0 = (\pi\epsilon_0)/\cosh^{-1}\left(\frac{s}{2a}\right), \tag{5.105}$$

where s is the distance between wire centers, and a is the radius of each wire. Using (5.103–5.105), we find that the impedance of our line is approximately $Z_0 = 407\ \Omega$. The true impedance can be determined numerically as

$$Z_0 = \sqrt{Z_{oc}Z_{sc}}, \tag{5.106}$$

where Z_{oc} and Z_{sc} are the input impedances with the load terminals opened and shorted, respectively. We must be careful, however, that we do not take the measurement at a frequency where the length of the line would result in an extremely small or large impedance at the input end, as numerical inaccuracy would result. We therefore make the measurement at a frequency of 15 MHz, where the length of the line

is approximately $\lambda/8$. Using the thin-wire EFIE with a delta-gap source, we find the impedance to be $Z_0 \approx 412\ \Omega$, which is close to the theoretical value.

We next compare the computed input impedance to that of an ideal lossless transmission line, which is [8]

$$Z_{in} = Z_0 \frac{Z_l + jZ_0 \tan(k_0 l)}{Z_0 + jZ_l \tan(k_0 l)}\,, \tag{5.107}$$

where Z_l is the load impedance, and Z_{in} the impedance measured at a distance l from the load. For the comparison, we use a load with a pure resistance of $200\ \Omega$. The results are plotted in Figure 5.19 for frequencies between 100 kHz and 100 MHz. The comparison is quite good. At lower frequencies, the input impedance tends toward the DC value, as expected.

Two-wire lines are only useful at frequencies where they are not effective radiators, which is typically satisfied when $s \ll \lambda$. Let us retain the $200\ \Omega$ load, and place the line in the xy plane with the feedpoint on the $-x$ axis. We then compute the real part of the radiated near electric field (in V/m) at 15 MHz in the xz plane, which is shown in Figure 5.20. We note that even though the load is not matched and there are standing waves on the line, the fields are concentrated in a small, tight region surrounding the line, with virtually no field radiated. Increasing the frequency to 500 MHz, we see in Figure 5.21 that the near field is no longer confined close to the line. Increasing the frequency further to 1 GHz, we observe in Figure 5.22 that the line is now clearly behaving as an antenna, making it unsuitable as a transmission line at this frequency.

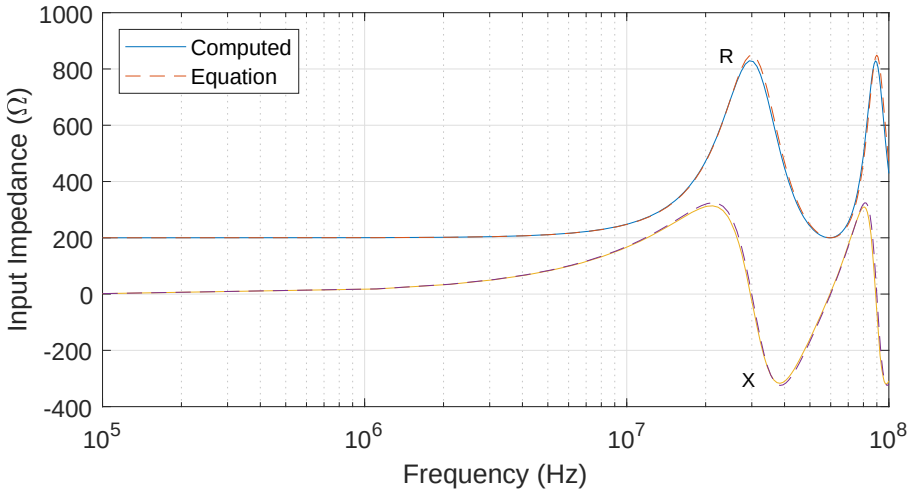


Figure 5.19: Two-Wire Line Input Impedance

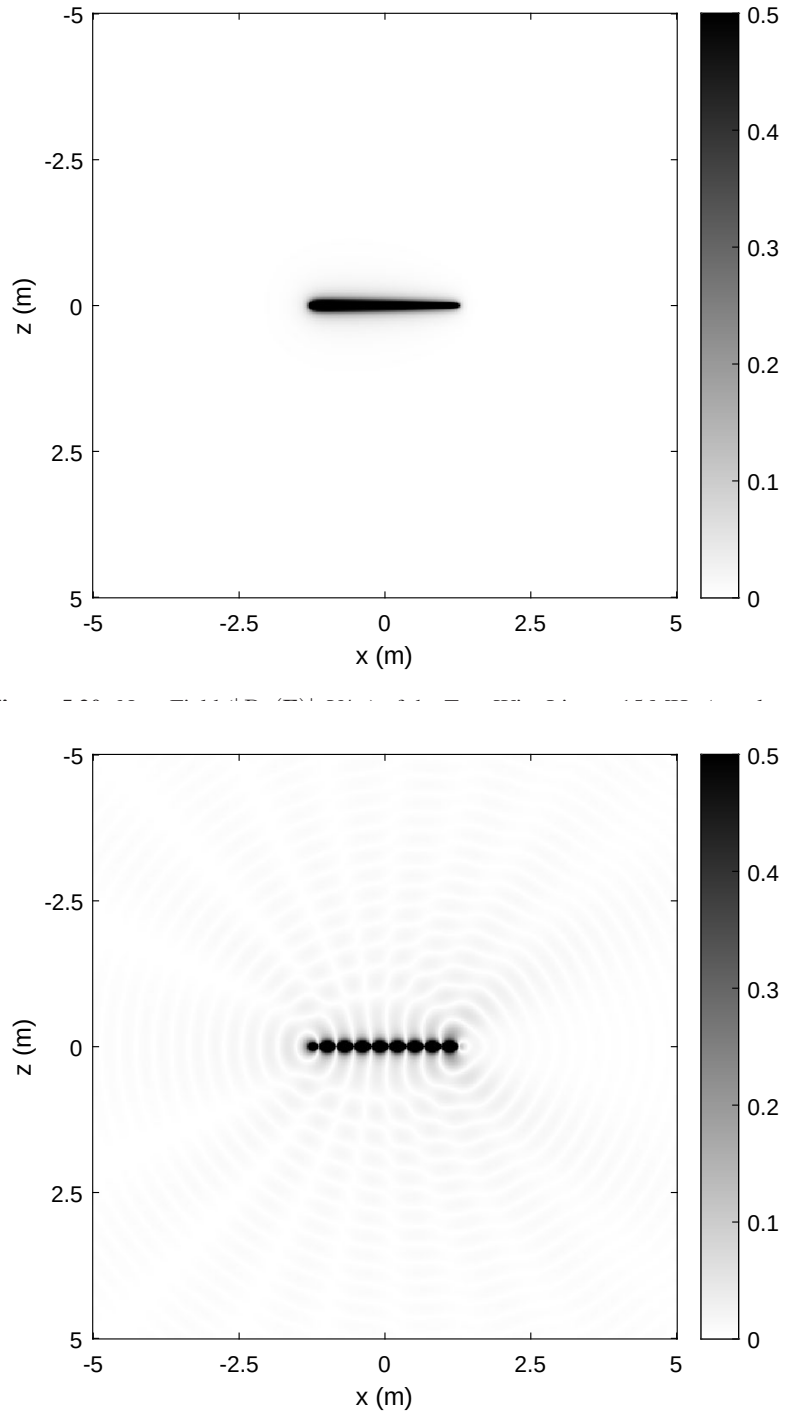


Figure 5.21: Near Field ($|\,\mathrm{Re}(\mathbf{E})|$, V/m) of the Two-Wire Line at 500 MHz (xz plane)

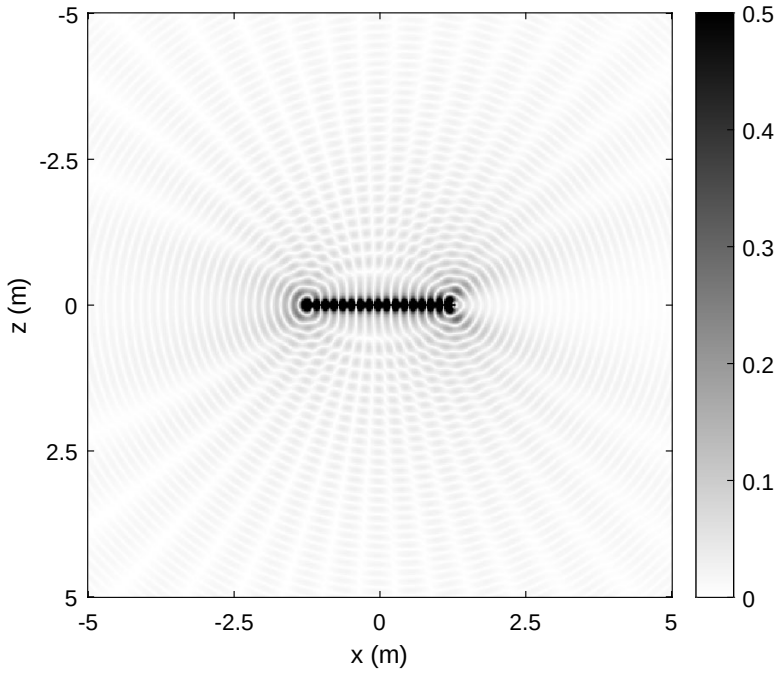


Figure 5.22: Near Field ($|\,\mathrm{Re}(\mathbf{E})|$, V/m) of the Two-Wire Line at 1 GHz (xz plane)

5.6.6 Yagi Antenna for 146 MHz

We now examine a more practical antenna: a Yagi antenna for the 2-meter amateur radio band (144–148 MHz). The dimensions and locations for the antenna elements are from [12] and are summarized in Table 5.1. The diameter for each element is 6.35 mm (1/4 inch). Our thin-wire EFIE model comprises separate straight wires in the xz plane, as shown in Figure 5.23. Each wire is assigned 25 segments. The feedpoint with delta-gap source is at the center of the *driven element*, noted with a dot in Figure 5.23. Though a real Yagi antenna would use a piece of metal or plastic tubing called a *boom* to affix the antenna elements, the boom does not typically have much current flow on it and we omit it from our analysis.

Most Yagi antennas have a single element placed behind the driven element called a *reflector*. This element reduces the amount of power radiated along the $-x$ axis in Figure 5.23 (the "back" side). The elements to the right of the driven element are called *directors*, and they act to focus or *direct* most of the power along the $+x$ axis (the "front" side). Though these elements are not connected to the feedline, they interact with the other elements via the near field, and are often referred to as *parasitic* elements.

The input resistance and reactance of the Yagi antenna over the 2-meter band are shown in Figures 5.24a and 5.24b, respectively. The antenna has a feedpoint resistance between 18 and 33 Ω over the band, and a capacitive reactance, which is typical of Yagi antennas. This antenna can be matched to a $50\ \Omega$ coaxial feed using a lumped inductive element at the feedpoint (a coil) or a tuning stub such as the hairpin match [13] and a 2:1 balun. We will match the antenna at about 146.5 MHz, where its reactance is approximately $-j18.8\ \Omega$. To achieve the match we follow Section 5.5.4, and place an inductance of about 20 nH at the feedpoint, which will remove the capacitive reactance.

Table 5.1: 2 Meter Yagi Antenna Parameters

Element	REF	DE	D1	D2	D3	D4	D5	D6	D7
Length (mm)	1038	955	956	932	916	906	897	891	887
x location (mm)	0	312	447	699	1050	1482	1986	2553	3168

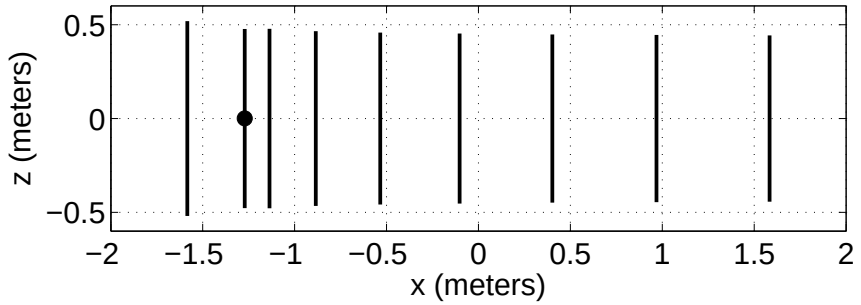


Figure 5.23: Yagi Antenna For the 2 Meter Amateur Radio Band

The reactance after matching is shown in Figure 5.25a. We next compute the standing wave ratio (SWR), a common way of describing how well an antenna is matched to the feedline. The SWR is computed as [8]

$$\text{SWR} = \frac{1 + |\Gamma_L|}{1 - |\Gamma_L|} \,, \tag{5.108}$$

where Γ_L is the reflection coefficient at the load, given by

$$\Gamma_L = \frac{Z_L - Z_0}{Z_L + Z_0} \,, \tag{5.109}$$

where Z_L is the load impedance. A perfectly matched antenna has an SWR $= 1$, indicating no power is reflected at the antenna terminals. An SWR ≥ 2 indicates a poor match and significant reflected power, and in high power applications, a mismatch can damage the transmitter's power amplifier. To account for the 2:1 balun, we use double the computed feedpoint impedance for the load impedance Z_L in (5.109). The SWR for the matched antenna is shown in Figure 5.25b, where a nearly perfect match is achieved at 146.5 MHz.

We next compute the front-to-back ratio, which comprises the ratio of the forward-broadside to rear-broadside radiated power. In the far field, the power density can be computed using the electric field $\mathbf{E}$ as

$$P = \frac{1}{2\eta_0} |\mathbf{E}|^2 \,. \tag{5.110}$$

Because the Yagi antenna only has $\hat{\mathbf{z}}$-oriented elements, the far radiated electric field along the x axis ($\theta = 90, \phi = 0, \pi$) has $\hat{\boldsymbol{\theta}}$-polarization only. The resulting front-to-back ratio is plotted in dB, versus frequency, in Figure 5.26a.

Finally, we compute the forward power gain G_i (relative to isotropically radiated power), which comprises the ratio of the forward broadside radiated power density to the average isotropic radiated power density P_{avg}. This average is computed as [8]

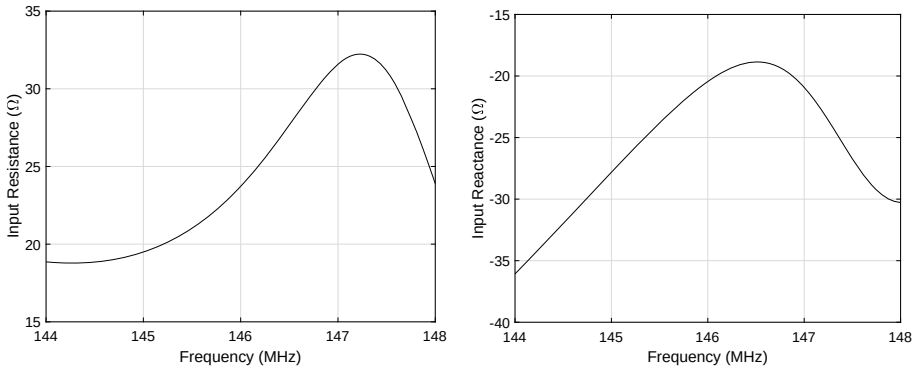
$$P_{avg} = \frac{P_{in}}{4\pi} = |I|^2 \frac{R_{in}}{4\pi} = \left| \frac{V_{in}}{Z_{in}} \right|^2 \frac{R_{in}}{4\pi} \,, \tag{5.111}$$

and so

$$G_i = \frac{P}{P_{avg}} = 2\pi \frac{|\mathbf{E}|^2 |Z_{in}|^2}{\eta R_{in}} \,, \tag{5.112}$$

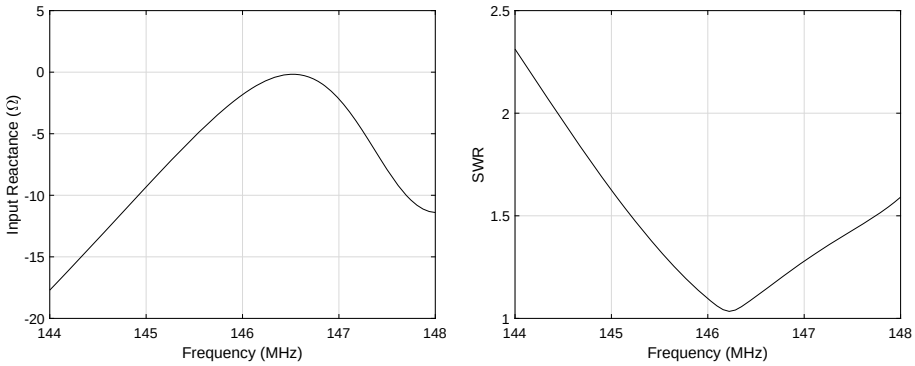
where $V_{in} = 1$. The gain is plotted in dBi (dB over isotropic) in Figure 5.26b, where the gain is fairly constant at about 10 dBi over the operating band.

We next consider the radiated near field in the xy plane. The real part of the total radiated near electric field in a 40×40 meter region around the antenna is shown in Figure 5.27a. The $\hat{\boldsymbol{\theta}}$-polarized far radiated field pattern is shown versus ϕ in Figure 5.27b. A similar plot of the near field in the xz plane is shown in Figure 5.28a. The corresponding $\hat{\boldsymbol{\theta}}$-polarized far radiated field pattern is shown versus θ in Figure 5.28b. The normalized total far field pattern on the unit sphere for all θ and ϕ is shown in Figure 5.29.



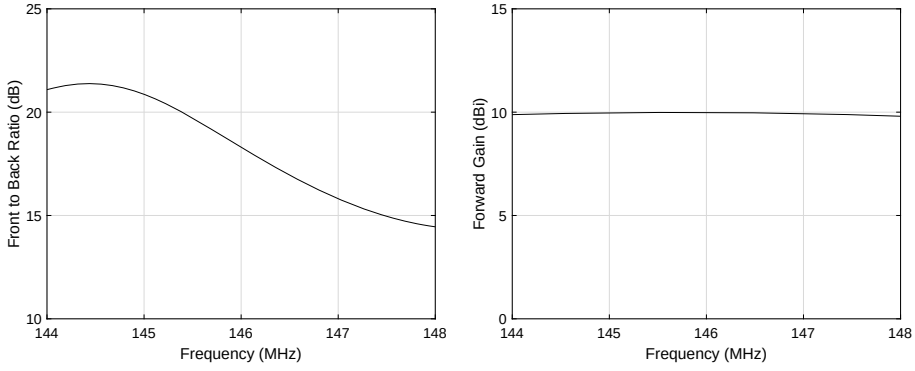
(a) Resistance (b) Reactance

Figure 5.24: Yagi Antenna Unmatched Impedance



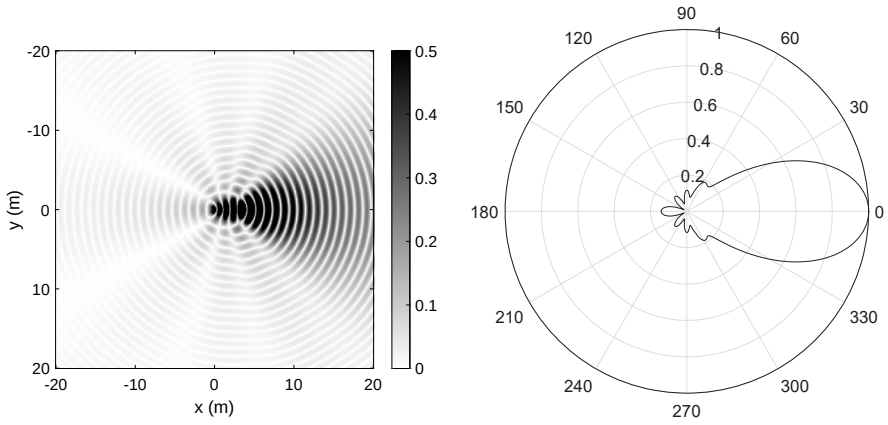
(a) Reactance (b) SWR ($Z_0 = 50\,\Omega$)

Figure 5.25: Yagi Antenna Matched Reactance and SWR



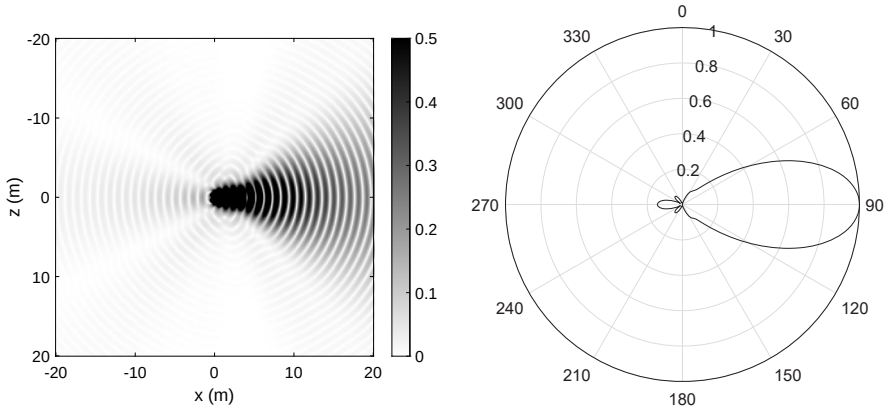
(a) Front to Back Ratio (b) Forward Gain

Figure 5.26: Yagi Antenna Performance Characteristics



(a) Near Field ($|\,\mathrm{Re}(\mathbf{E})|$, V/m) (b) Normalized Far Field Amplitude

Figure 5.27: Radiated Field of the Yagi Antenna (xy plane)



(a) Near Field ($|\,\mathrm{Re}(\mathbf{E})|$, V/m) (b) Normalized Far Field Amplitude

Figure 5.28: Radiated Field of the Yagi Antenna (xz plane)

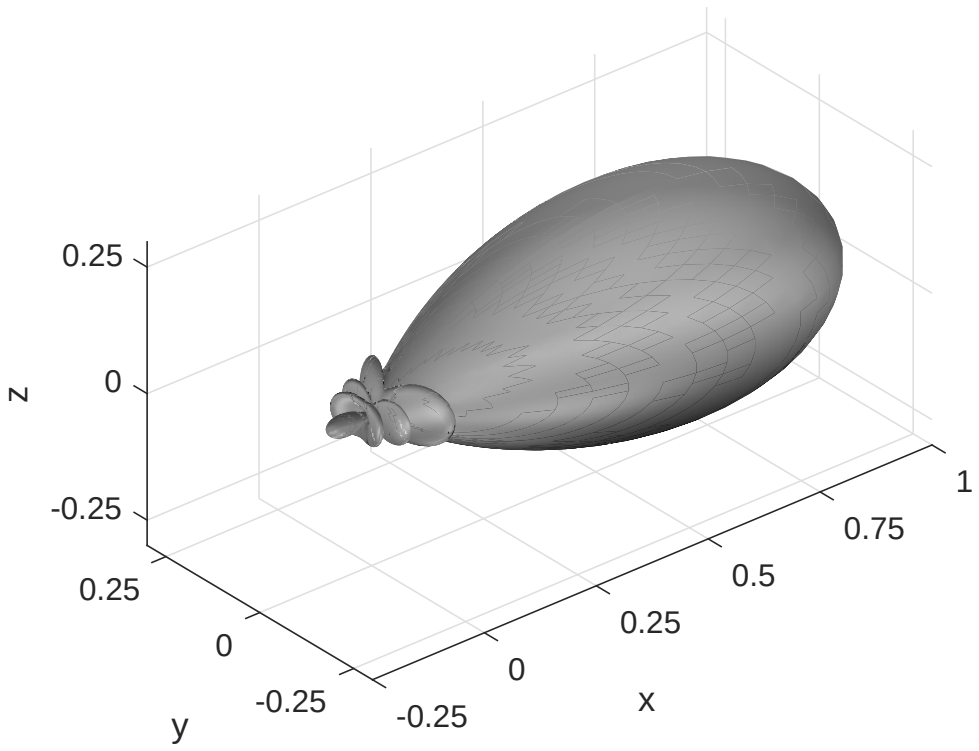


Figure 5.29: 3D Far Field Pattern of Yagi Antenna

References

[1] R. W. P. King, "The linear antenna – Eighty years of progress," *Proc. IEEE*, vol. 55, pp. 2–26, January 1967.

[2] W. Wang, "The exact kernel for cylindrical antenna," *IEEE Trans. Antennas Propagat.*, vol. 39, pp. 434–435, April 1991.

[3] D. R. Wilton and N. J. Champagne, "Evaluation and integration of the thin wire kernel," *IEEE Trans. Antennas Propagat.*, vol. 54, pp. 1200–1206, April 2006.

[4] E. Hallén, "Theoretical investigations into the transmitting and receiving qualities of antennae," *Nova Acta (Uppsala)*, vol. 11, pp. 1–44, 1938.

[5] H. C. Pocklington, "Electrical oscillations in wires," *Proc. Camb. Phil. Soc.*, vol. 9, 1897.

[6] W. Stutzman and G. Thiele, *Antenna Theory and Design*. John Wiley and Sons, 1981.

[7] C. A. Balanis, *Advanced Engineering Electromagnetics*. John Wiley and Sons, 1989.

[8] S. J. Orfanidis, "Electromagnetic waves and antennas." Electronic version: ece.rutgers.edu/ orfanidi/ewa/.

[9] H. B. Dwight, *Tables of Integrals and Other Mathematical Data*. The Macmillan Company, 1961.

[10] *The Integrator*. Wolfram Research, integrals.wolfram.com.

[11] C. A. Balanis, *Antenna Theory: Analysis and Design*. John Wiley and Sons, second ed., 1997.

[12] *The ARRL Antenna Book*. The Amateur Radio Relay League, 17th ed., 1994.

[13] W. Orr, *Radio Handbook*. Sams, 1992.